Design Strategies to Achieve Target Collapse Risks for RC-Wall Buildings in Sedimentary Basins

Nasser A. Marafi[1], Andrew J. Makdisi[2], Jeffrey W. Berman[3], and Marc O. Eberhard[4]

Studies of recorded ground motions and simulations have shown that deep sedimentary basins can greatly increase the damage expected during earthquakes. Unlike past earthquake design provisions, future ones are likely to consider basin effects, but the consequences of accounting for these effects are uncertain. This paper quantifies the impacts of basin amplification on the collapse risk of 4- to 24-story reinforced concrete wall building archetypes in the uncoupled direction. These buildings were designed for the seismic hazard level in Seattle according to the ASCE 7-16 design provisions, which neglect basin effects. For ground motion map frameworks that do consider basin effects (2018 USGS National Seismic Hazard Model), the average collapse risk for these structures would be 2.1% in 50 years, which exceeds the target value of 1%. It is shown that this 1% target could be achieved by: (a) increasing the design forces by 25%; (b) decreasing the drift limits from 2.0% to 1.25%; or (c) increasing the median drift capacity of the gravity systems to exceed 9%. The implications for these design changes are quantified in terms of the cross-sectional area of the walls, longitudinal reinforcement, and useable floor space. It is also shown that the collapse risk increases to 2.8% when the results of physics-based ground motion simulations are used for the large-magnitude Cascadia subduction interface earthquake contribution to the hazard. In

[1]Postdoctoral Research Associate, Department of Civil and Environmental Engineering, University of Washington, Seattle, WA 98195

[2]Graduate Research Assistant, Department of Civil and Environmental Engineering, University of Washington, Seattle, WA 98195

[3]Professor, Department of Civil and Environmental Engineering, University of Washington, Seattle, WA 98195

[4]Professor, Department of Civil and Environmental Engineering, University of Washington, Seattle, WA 98195

this case, it is necessary to combine large changes in the drift capacities, design forces and/or drift limits to meet the collapse risk target.

Keywords: Deep sedimentary basin effects, reinforced concrete walls, nonlinear dynamic analysis, long duration motions, Cascadia Subduction Zone

Introduction

Deep sedimentary basins underlie some of the largest metropolitan regions in the Western United States, including the Puget Sound region, as well as parts of the Los Angeles, San Francisco Bay Area, and Salt Lake City regions. Such basins are known to amplify ground-motion components in long-period ranges (e.g., 1-4 s), resulting in increased spectral accelerations (e.g., Choi et al., 2005) and more damaging spectral shapes (Marafi et al., 2017), which combined, increase the likelihood of collapse during an earthquake (e.g., Heaton et al., 2006, Bijelic, 2018, Marafi et al., 2019c). As opposed to past versions of the National Seismic Hazard Model, the most recent version (NSHM, USGS 2018) accounts for the effect of basins on spectral acceleration. The adoption of the new hazard model into the code provisions (e.g., ASCE 7, AASHTO) would result in large increases in design spectral accelerations for structures located on deep basins.

The design spectral accelerations in the ASCE 7-16 provisions are derived from the 2014 NSHM, which does not consider the effects of deep basins. In this paper, the collapse risk for ASCE 7-16 code-compliant building archetypes is investigated for the increased spectral accelerations from the updated 2018 NSHM. These consequences are calculated for a series of previously designed reinforced concrete wall archetypes ranging from four to twenty-four stories. The archetypes were designed for the seismic hazard in Seattle, met the minimum code requirements set by ASCE 7-16, and are referred to as *reference archetypes* throughout this paper. Previous work by the authors (Marafi et al., 2019c) showed that, if basin effects were considered, the conditional collapse probability for ASCE 7-16 archetypes averaged 21% for an **M**9 event on the Cascadia Subduction Zone with a return period of approximately 526 years (Petersen et al., 2014). This paper extends the previous work in three ways:

(1) The 50-year collapse risk was computed for each of the reference archetypes for the 2014 and 2018 NSHMs. To compute this risk, a multiple stripe analysis (MSA, Jalayer and Cornell, 2009) was conducted for each archetype; the intensity stripes corresponded to the spectral amplitude at a given archetype's fundamental period

($S_a[T_1]$) with return periods of 100, 475, 975, 2,475, and 4,975 years. Each intensity stripe within the MSA consisted of ground motions that were selected and scaled to a source-specific (i.e., crustal, intraslab, and interface) conditional spectrum (Jayaram et al., 2011) for that particular $S_a(T_1)$ return period and NSHM version. The resulting collapse probabilities are compared to the 1% in 50-year collapse risk target set by the ASCE 7-16 design provisions.

(2) The paper evaluates the effectiveness of implementing four strategies to redesign the reference archetypes to reduce the seismic collapse risk for the 2018 NSHM demands. The strategies are: (1) increasing the seismic response coefficient (C_s) in ASCE 7-16 by 25% or by 50%, (2) reducing the design drift limits prescribed in ASCE 7-16 from 2.0% to 1.5% or 1.25%, (3) increasing the drift capacity of the gravity system, and (4) combining changes in strength or drift limits with increases in drift capacity. The implications of adopting these design strategies are quantified in terms of the cross-sectional area of the walls, longitudinal reinforcement, and useable floor space.

(3) Finally, the results of physics-based ground-motion simulations for 30 scenarios of a full rupture of the Cascadia Subduction Zone (Frankel et al 2018) are incorporated into the risk assessment. The simulations are used to compute the likelihood of collapse during an **M**9 earthquake; MSA is used to assess the collapse risk for the other earthquake magnitudes and sources, and the combined risk is computed.

To provide context for interpreting these new findings, the following sections summarize previous work by ground-motion modeling researchers that quantified the effects of basins, and how engineers are beginning to account for basin effects in building design.

Observations of Basin Effects on Ground Motions

Many researchers have shown that recorded motions have spectral accelerations that are larger in deep sedimentary basins than in surrounding locations. Choi et al. (2005) quantified these amplifications and developed an empirical model that accounts for the depth of the basin and the location of the source relative to the basin. More recent ground-motion models that are part of NGA-West2 (Bozorgnia et al., 2014) have included terms that account for deep sedimentary basins during crustal earthquakes. Similar trends were found for subduction earthquakes. For example, Morikawa and Fujiwara (2013) and Marafi et al. (2017) quantified the amplification of spectral accelerations by basins during interface and intraslab earthquakes in Japan.

The effects of deep sedimentary basins on ground-motion characteristics have also been observed in physics-based simulations of earthquake ground motions. For example, Aagaard et al. (2010) simulated 39 Hayward Fault scenarios (**M**6.7 to **M**7.2) and found that the shaking intensity increased within the basins near the San Francisco Bay Area (e.g., Cupertino basin, Livermore basin). Graves et al. (2011) simulated numerous earthquakes as part of the Uniform California Earthquake Forecast model (UCERF) and found that the ground-motion intensities increased for sites within the Los Angeles basin. Moschetti et al. (2017) simulated **M**7 earthquakes on the Salt Lake City segment of the Wasatch Fault zone and found that the long-period ground-motion intensity increased for deep basin sites in the Wasatch basin. Recently, Frankel et al. (2018) and Wirth et al. (2018a) simulated **M**9 earthquakes on the Cascadia Subduction Zone (CSZ) and found that ground-shaking intensity is amplified for periods from 1 s to 4 s for locations in basins within the Puget Lowland region, which includes Seattle.

Accounting for Basin Effects in Structural Design

Engineers have begun to account for the effects of basins on spectral acceleration. For example, the Southern California Earthquake Center (SCEC) developed site-specific, risk-adjusted, maximum considered earthquake (MCE_R) spectra for the metropolitan Los Angeles area that consider the effects of basins, predicted using empirical ground-motion models and 3D physics-based simulations (using the CyberShake computational platform, Crouse et al., 2018). The City of Seattle (Director's Rule 5, 2015) required that basin effects be considered within performance-based design (PBD) procedures for buildings above 73 m (240 ft) without a dual lateral-force resisting system (Chang et al., 2013). The basin amplification factors were then increased and applied to all projects that use a site-specific hazard analysis in 2018 (Director's Rule 20, 2018, Wirth et al., 2018b).

The preliminary 2018 update of the National Seismic Hazard Model (USGS, 2018), denoted here as 2018 NSHM, extends the treatment of basins to a national level. Specifically, a recent USGS report (USGS, 2018) proposes that the effects of sedimentary basins be considered for the Seattle, Los Angeles, San Francisco Bay Area, and Salt Lake City regions. Figure 1 shows the extents of the basins considered in the 2018 NSHM. The new seismic hazard model accounts for basin effects on spectral acceleration for all earthquake sources using basin terms adapted from the crustal earthquake ground-motion models in the NGA-West2 project (Bozorgnia et al., 2014).

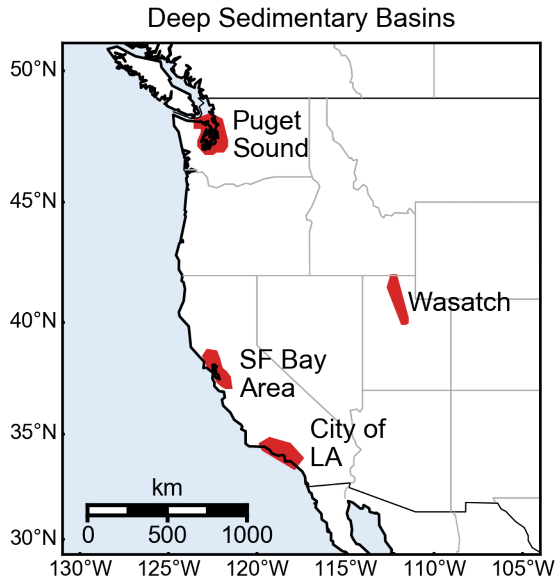

Figure 1. Extent of deep sedimentary basins (as per USGS 2018) that are taken into account by the 2018 National Seismic Hazard Model.

For many locations, the inclusion of basin effects increased the spectral acceleration values in the 2018 NSHM compared to the 2014 values. Table 1 lists values of the spectral accelerations (at periods of 0.2 s, 1.0 s, and 2.0 s) corresponding to a 2% likelihood of exceedance in 50 years (2,475-year return period), as determined from the 2014 and 2018 NSHMs (USGS 2014, USGS 2018), for V_{s30} = 500 m/s (Site Class C). The values are reported for locations inside and outside basins (or near the shallower parts of the basin) for the four regions identified in the 2018 USGS report (Figure 1). For example, the values from the 2018 NSHM S_a at a period of 2.0 s exceeded the corresponding 2014 values for Seattle, Compton, Pleasanton, and Salt Lake City by 66%, 30%, 29%, and 15%, respectively. In contrast, for nearby locations outside the basins or near the shallower parts of the basins, the changes in S_a values were all less than 12%. In addition, the change in S_a values within the basins were much smaller at short periods (e.g., 0.2 s) [+15%, +0%, -1%, and -4%].

A common proxy for basin depth is the depth from the surface to a layer with a shear-wave velocity of at least 1.0 km/s or 2.5 km/s, denoted as $Z_{1.0}$ and $Z_{2.5}$, respectively. Compared to the other basins, Seattle has the largest values of $Z_{2.5}$, which are equal to 6.9 km, respectively (Table 1). Figure 2 shows the uniform hazard spectra (UHS) in the orientation corresponding to median spectral acceleration values for Seattle for a 2% probability of exceedance in 50 years for Site Class C. This value, often denoted as $S_{a,RotD50}$, will be referred to as S_a throughout the paper. As shown in Figure 2, the increases between the 2014 and 2018 NSHM occur over a wide range of periods. The increases are on average approximately 25% for periods below 0.45 s, and the average increase is approximately 50% for periods between 0.45 s and 1.71 s. This period range corresponds approximately to typical periods of 4- to 24-story reinforced concrete wall buildings designed as per ASCE 7-16 (Marafi et al., 2019c). The increase is largest at a period of 4 s, where S_a increases from 0.13 g to 0.22 g, corresponding to an increase of 72%. However, at this period, the design base shear (ASCE 7-16) is governed by the minimum base-shear requirements.

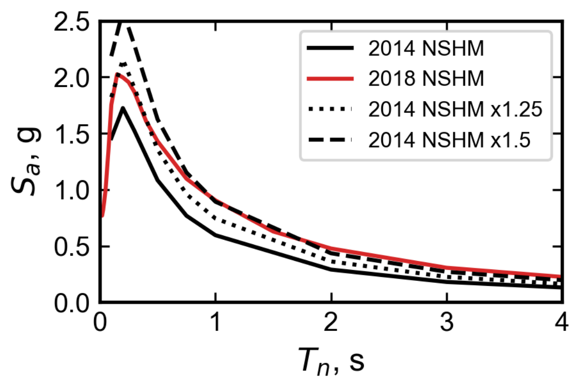

Figure 2. Uniform hazard spectra for a 2% probability of exceedance in 50 years in the direction corresponding to median spectral acceleration (RotD50) for Seattle computed using the USGS (2019) probabilistic seismic hazard analysis code.

Table 1. Uniform Hazard Spectral Accelerations (2% probability of exceedance in 50-years) for V_{S30} = 500 m/s (Site Class C)

						2014 NSHM			2018 NSHM		
Region	Location	Inside/ Outside Basin	Lat., Long.	$Z_{1.0}$, km	$Z_{2.5}$ km	S_a (0.2s), g	S_a (1.0s), g	S_a (2.0s), g	S_a (0.2s), g	S_a (1.0s), g	S_a (2.0s), g
Puget Sound	Seattle, WA	Inside	47.60°N, -122.30°W	0.9[e]	6.7[a]	1.74	0.60	0.29	2.00	0.90	0.48
	La Grande, WA	Outside	46.84°N, -122.32°W	0.0[a]	0.0[a]	1.48	0.51	0.25	1.47	0.54	0.28
City of LA	Compton, CA	Inside	33.90°N, -118.22°W	0.7[b]	4.3[b]	2.09	0.80	0.36	2.09	0.96	0.47
	Los Angeles, CA	Outside	34.05°N, -118.25°W	0.3[b]	2.1[b]	2.35	0.93	0.41	2.32	0.98	0.44
SF Bay Area	Pleasanton, CA	Inside	37.70°N, -122.93°W	0.6[c]	4.3[c]	2.69	1.09	0.49	2.66	1.28	0.63
	San Francisco, CA	Outside	37.75°N, -122.40°W	0.0[c]	0.9[c]	2.16	0.91	0.46	2.08	0.93	0.47
Wasatch	Salt Lake City, UT	Inside	40.75°N, -111.90°W	0.5[d]	2.8[d]	1.98	0.77	0.33	1.90	0.84	0.38
	West Jordan, UT	Outside	40.60°N, -112.00°W	0.0[d]	2.7[d]	1.36	0.50	0.22	1.32	0.51	0.23

Notes: [a]$Z_{1.0}$ and $Z_{2.5}$ values were obtained from Stephenson et al. (2017). [b]$Z_{2.5}$ values were obtained from SCEC Community Velocity Model (CSM-S4.26, Small et al., 2017). [c]$Z_{1.0}$ and $Z_{2.5}$ values were obtained from the USGS San Francisco Bay Area Seismic Velocity Model (Aagard 2019). [d]$Z_{1.0}$ and $Z_{2.5}$ values were obtained from Moschetti et al. (2018). [e]$Z_{1.0}$ values modified based on USGS Report (2018). Note that all spectral accelerations are in the orientation that corresponds to the median spectral acceleration for each period (RotD50).

Archetype Designs

The effects of changes in design spectra between the 2014 and 2018 versions of the USGS hazard models were evaluated for modern mid- and high-rise reinforced concrete core-wall archetypal residential buildings, ranging from 4 to 24 stories. To reflect current practice in Seattle, all of the archetypes were designed and detailed as special reinforced concrete shear walls (Chapter 18 of ACI 318-14), with a seismic force-reduction factor, R, of 6. The archetypes were developed with extensive input from design professionals, following the same design methodology detailed in Marafi et al. (2019c). Buildings with a height above 73 m (240 ft) are not considered in this paper, because the design of such buildings in Seattle is subject to extensive peer review, which accounts for the effects of the Seattle basin.

Figure 3a shows typical floor plans for the archetypes. The floor plate was 30.5 m (100 ft.) long by 30.5 m (100 ft.) wide with three, 9.15-m (30-ft.) bays of slab-column gravity framing in each orthogonal direction. The 4-story archetypes had two planar walls in each orthogonal direction. Archetypes with 8 stories or more used a central core-wall archetype that was symmetrical in both directions, in which one direction used two uncoupled C-shaped walls, whereas the other direction used coupled C-shaped walls. As is typical for residential buildings, the 4- and 8-story archetypes included two and three basement levels, respectively, and the taller archetypes had four basement levels. The basements were assumed to have plan dimensions of 48.8 m x 48.8 m (160 ft x 160 ft) (Figure 3b). The floor-to-floor heights for all stories (basement levels included) were 3.05 m (10 ft).

All core-wall archetypes were designed and detailed according to Chapter 18 in ACI 318-14. The core wall concrete was assumed to have a specified compressive strength (f'_c) of 55.2 MPa (8,000 psi) and reinforced with steel with nominal yield stress (f_y) of 414 MPa (60 ksi).

Six reference archetypes (4, 8, 12, 16, 20, and 24 stories) were designed to meet the minimum prescriptive, equivalent-lateral-force (ELF) requirements of ASCE 7-16 (2017), following the modal response spectrum analysis (MRSA) procedure. These provisions refer to the 2014 NSHM ground-motion values. The maximum allowable drift for these archetypes was 2% for the design earthquake loads, and the flexural demand-to-capacity ratio was selected to be near 1.0 at the ground floor. Key properties of these reference archetypes are provided in Table 2, in which the reference archetypes are denoted by their number of stories (e.g., S8) and with the additional designation of "-REF".

For each of these six archetypes, the impacts of adopting four design strategies were studied. As part of Design Strategy #1, archetypes were redesigned for lateral loads that are 25% or 50% larger than $S_{a,MCE}$ computed using the 2014 NSHM (denoted with -S125 or -S150). As part of Design Strategy #2, archetypes were redesigned to meet a stricter story drift target of 1.5% or 1.25% (denoted with -D150 or -D125), as opposed to the current ASCE 7-16 value of 2.0%. Design Strategy #3 assumed no changes to the reference designs of the seismic force resisting system, but it assumed that the gravity system could be redesigned to have a larger drift capacity. Design Strategy #4 combined the archetype redesigns with increased strength

(Design Strategy #1) or stricter drift limit (Design Strategy #2) with improvements in the ductility of the gravity system (Design Strategy #3).

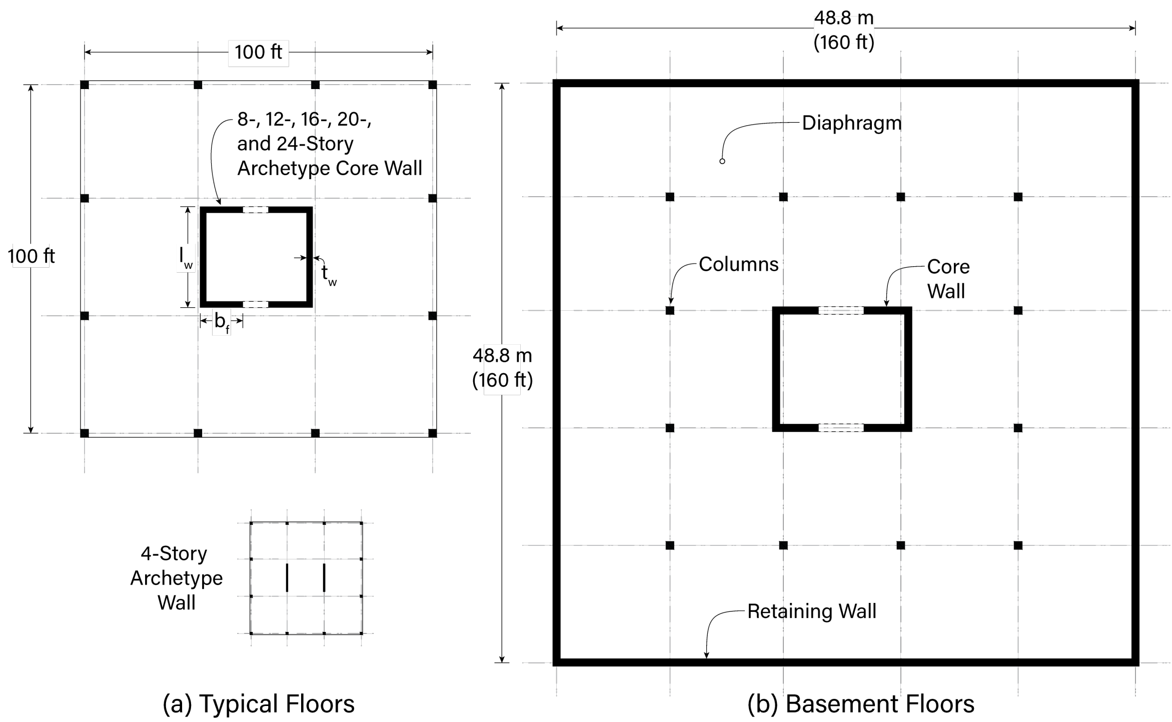

Figure 3. Plan view of archetypes at: (a) typical floors and (b) basement floors.

Table 2 lists the key properties for all of the archetype buildings. The resulting seismic weights per unit floor area (excluding the basement levels) ranged from 8.27 kPa (173 psf) for the 12-story reference archetype (S12-REF) to 9.91 kPa (207 psf) for the 24-story archetype with a 50% increase in design lateral forces (S24-S150). The increase in weight per unit floor area with respect to archetype stories is attributed to the increase in wall dimensions. Table 2 lists the upper limit on the design period ($C_u T_a$) used to compute C_s and the computed fundamental period (T_1) with cracked concrete properties used in the modal analysis. The total base shear, expressed as a percentage of the total building weight (C_s), ranged from 4.9% to 27.4%, depending on the archetype height and design strategy. The minimum base shear requirement in ASCE 7-16 controlled the strength of the archetypes with 24 stories.

Table 2. Key archetype properties

Performance Group	Arch. ID	# of Stories (Basements)	C_uT_a (s)	Computed Period, T_1[1] (s)	C_s	W[2] (MN)	$\phi M_n/M_u$[3]	V_u/V_c[3]	Drift Ratio (%)	Axial Load Ratio (P_g/f'_cA_g)
Reference	S4-REF	4(2)	0.45	1.08	0.183	30.9	1.05	1.74	1.82	0.11
(ASCE 7-16)	S8-REF	8(3)	0.75	1.93	0.109	61.8	1.06	1.49	1.8	0.10
	S12-REF	12(4)	1.02	2.70	0.08	92.3	1.01	1.32	1.89	0.11
	S16-REF	16(4)	1.26	3.53	0.065	125.1	1.03	1.05	1.96	0.11
	S20-REF	20(4)	1.49	4.36	0.055	158.5	1.05	0.92	2.03	0.11
	S24-REF	24(4)	1.71	5.11	0.049[4]	195.0	1.04	0.85	2.00	0.11
Reference	S4-S125	4(2)	0.45	0.95	0.228	31.1	1.06	1.80	1.95	0.09
w/ x1.25 Design Forces	S8-S125	8(3)	0.75	1.57	0.136	62.6	1.05	1.65	1.84	0.08
	S12-S125	12(4)	1.02	2.12	0.100	94.0	1.08	1.38	1.87	0.09
	S16-S125	16(4)	1.26	2.36	0.081	132.3	1.04	0.90	1.86	0.08
	S20-S125	20(4)	1.49	2.58	0.068	171.1	1.07	0.69	1.93	0.07
	S24-S125	24(4)	1.71	2.78	0.062	213.4	1.06	0.60	1.97	0.07
Reference	S4-S150	4(2)	0.45	0.78	0.274	31.4	1.06	1.79	1.95	0.07
w/ x1.50 Design Forces	S8-S150	8(3)	0.75	1.41	0.163	63.4	1.04	1.68	1.90	0.07
	S12-S150	12(4)	1.02	2.02	0.12	95.8	1.07	1.29	1.95	0.08
	S16-S150	16(4)	1.26	2.22	0.097	134	1.05	1.04	1.93	0.07
	S20-S150	20(4)	1.49	2.38	0.082	175.3	1.06	0.74	1.92	0.07
	S24-S150	24(4)	1.71	2.56	0.074	221.0	1.08	0.63	1.95	0.06
Reference	S4-S150	4(2)	0.45	0.89	0.183	31.4	1.08	1.22	1.46	0.08
w/ 1.5% Design Drift Limit	S8-D150	8(3)	0.75	1.57	0.109	62.6	1.04	1.32	1.47	0.08
	S12-D150	12(4)	1.02	2.24	0.08	93.7	1.06	1.09	1.53	0.09
	S16-D150	16(4)	1.26	2.72	0.065	127.9	1.05	0.81	1.53	0.08
	S20-D150	20(4)	1.49	3.20	0.055	163.9	1.06	0.66	1.5	0.08
	S24-D150	24(4)	1.71	3.75	0.049[4]	200.7	1.06	0.60	1.51	0.08
Reference	S4-D125	4(2)	0.45	0.78	0.183	31.7	1.11	1.02	1.29	0.06
w/ x1.25% Design Drift Limit	S8-D125	8(3)	0.75	1.43	0.109	63.0	1.06	1.21	1.30	0.08
	S12-D125	12(4)	1.02	1.90	0.080	94.8	1.07	0.85	1.24	0.08
	S16-D125	16(4)	1.26	2.38	0.065	129	1.07	0.75	1.34	0.08
	S20-D125	20(4)	1.49	3.11	0.055	161.3	1.08	0.90	1.32	0.10
	S24-D125	24(4)	1.71	3.81	0.049[4]	193.8	1.07	1.02	1.36	0.13

Notes: [1]Period computed using cracked concrete properties, [2]Building seismic weight only includes stories above the ground floor, [3]computed at ground level and adjusted design forces, [4]Minimum base shear controls.

The resulting ratio of horizontal shear force (due to seismic loads) to the concrete shear capacity, V_u/V_c, ranged from 0.6 to 1.8, which is far below the allowable values (i.e., $V_u/V_c \leq 5$). Table 1 lists the resulting axial load ratios, $P_g/(A_g f'_c)$, where P_g is the axial load computed using the 1.0D + 0.5 L load combination, and A_g is the gross cross-sectional area of the wall. The axial load P_g was computed as the sum of the self-weight of the concrete core and the gravity load corresponding to the tributary area resisted by the core, assumed to equal 50% of the total floor area, equaling 464 m^2 (5000 ft^2). The resulting axial load ratios ranged from 6% to 13%. Appendix Tables 1-4 provide more information regarding the archetype geometry and reinforcement ratios.

Archetype Modelling

The seismic performance of all of the archetypes was assessed using 2D nonlinear models in *OpenSees* (McKenna, 2016) with the help of the computational resources provided by *DesignSafe-CI* (Rathje et al., 2016). These models did not account for the effects of torsion and bidirectional loading on structural response and only analyzed the response of the walls in the uncoupled direction (North-South orientation in Figure 3). The nonlinear behavior of the wall was modeled using a methodology that was developed by Pugh et al. (2015) and Marafi et al. (2019a), which uses displacement-based, beam-column elements with lumped-plasticity fiber sections to capture the axial and flexural nonlinear responses of the RC walls. The stress-strain behavior of the steel fibers includes cyclic strength degradation (Kunnath et al., 2009) to account for strength deterioration expected with long-duration shaking. The model methodology uses an elastic shear model and does not account for shear-flexure interaction. Rebar buckling was accounted for by assuming that the rebar buckles and loses its entire strength once the concrete reaches its the crushing strain. Marafi et al. (2019c) provide more details of the modeling strategy.

The numerical models did not include the lateral-force resistance of the gravity system, because the stiffness and strength contributions of the gravity system are usually much lower than that of the lateral system. It should be noted that the gravity system can contribute ~10% of the total lateral resistance of the building in some circumstances (SEAW Earthquake Engineering Committee meeting, personal communication, 2018, January 9th).

Multiple Stripe Analysis

The performance of each archetype was assessed using a multiple stripe analysis (Jalayer and Cornell, 2009), in which the collapse probability was quantified at multiple intensity measure levels, each corresponding to a particular return period. The intensity measure used in the MSA was the spectral acceleration (S_a) at the fundamental period (T_1) of each structural archetype, $S_a(T_1)$. The intensity stripes used in the MSA had return periods of 100, 475, 975, 2,475, and 4,975 years. The variety in return periods made it possible to account for the effects of ground motions for a wide range of earthquake intensities, ranging from low-intensity events that occur more frequently (i.e., lower return period) to high-intensity events that occur less frequently (i.e., longer return period). The probability of collapse results from each intensity level and corresponding earthquake return period was then integrated over the overall $S_a(T_1)$ hazard curve to estimate the probability of building collapse over a period of 50 years.

Conditional Mean Spectra

For each of the five return periods (100 through 4,975 years) and three types of source mechanism (crustal, interface, and intraslab), ground motions were selected and scaled to match a conditional mean and variance spectrum (Jayaram et al., 2011a). A conditional mean spectrum (CMS) is meant to represent the expected ground motion response spectrum conditioned on the occurrence of a target S_a at the computed fundamental period (T_1) of the archetype (Table 2).

For each of the 15 combinations of return period and type of source mechanism, the CMS at each conditioning period (Baker, 2011) was computed using the hazard deaggregation results from the 2014 and 2018 NSHM codes (USGS, 2019) for the downtown Seattle location. The CMS at each conditioning period was calculated as a weighted average (in log-scale) of the CMS for each ground-motion model and particular seismic source (e.g., Seattle fault) according to its percentage contribution to the hazard. These contributions are reported by the deaggregation results computed using the NSHM code (USGS, 2019). The spectral acceleration correlation functions used to calculate the CMS were assumed to be the same for crustal, intraslab, and subduction earthquakes (Jayaram et al., 2011b, Baker and Jayaram, 2008).

Figure 4 shows the 2-s period CMS for each source mechanism for earthquake return periods of 100, 475, 975, 2475, and 4,975-years for the 2018 NSHM. This range of earthquake return periods are necessary to constrain the collapse prediction, and thus account for low-intensity shaking (0.06 g at 100-year level shaking) where structural collapse is less likely, and at high-intensity shaking (0.64 g at 4,975-year level) where structural collapse is more likely.

Selection of Motions

To capture the inter-event uncertainty in the conditional mean spectra, motions were selected and scaled to match the target mean and variance conditional spectra (Jayaram et al., 2011), referred as the conditional spectra thereafter. As an example, Figure 5 shows the response spectra for 100 motions selected to represent the three types of earthquake source mechanisms for a 2,475-year return earthquake response spectra conditioned at a period of 2.0 s. Motions were selected to have spectral ordinates that are within two standard deviations of the target conditional mean spectra whilst achieving the target mean S_a and target variance at each period.

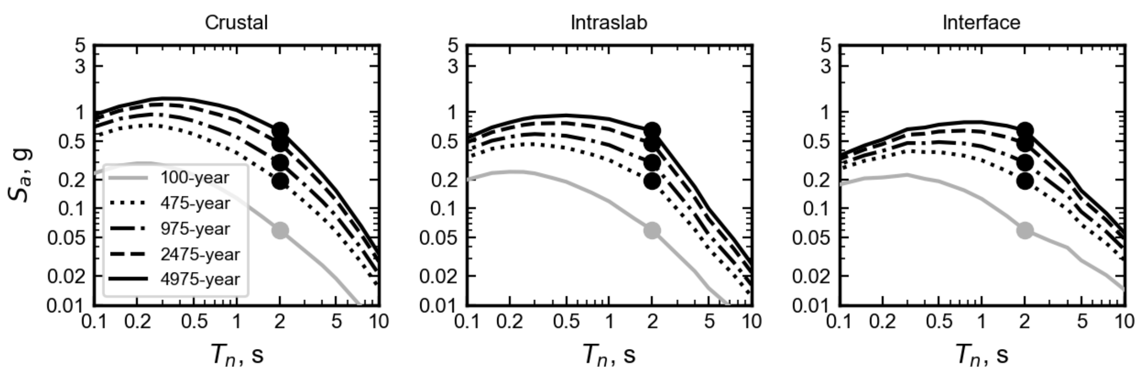

Figure 4. Conditional mean spectra at 2-second period (RotD50) for: (a) crustal, (b) intraslab, and (c) interface earthquakes at the 100-year, 475-year, 975-year, 2475-year, and 4975-year hazard levels according to the 2018 National Seismic Hazard Model.

Using the hazard deaggregation results for each type of source mechanism, motions recorded from crustal, intraslab, and interface earthquakes were included in each ground motion set in proportion to their contribution to the overall seismic hazard at each period. For example, for a period of 2.0 s and a return period of 475 years, the contributions of the crustal, intraslab, and interface sources were 29%, 20%, and 51%, respectively. At a return period of 2,475 years, the corresponding contributions were 27%, 7%, and 66%. To be consistent with the 2,475-year hazard deaggregation, Figure 5 (2.0 s conditional spectra) shows that 27, 7, and 66 motions were used to represent the contribution of the crustal, intraslab and interface events, respectively. Marafi (2018) provides further details of the ground-motion selection and scaling process.

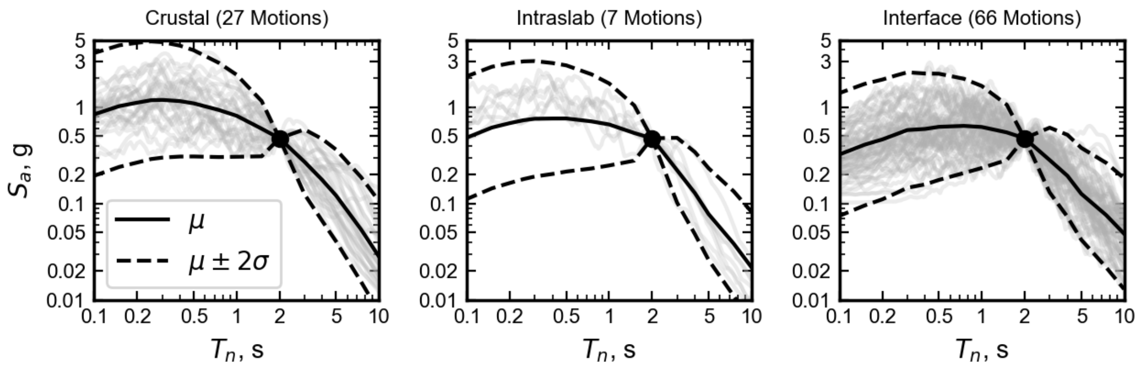

Figure 5. Ground motions scaled to match the 2.0-second period conditional mean and variance spectra for: (a) crustal, (b) intraslab, and (c) interface earthquakes at a 2475-year hazard level using the 2018 National Seismic Hazard Model.

Maximum Story Drift

For each of the archetypes and for each of the five earthquake intensity levels (corresponding to return period of 100 years to 4975 years), the maximum story drifts (MSDs) were computed for both the 2014 and 2018 NSHM hazard levels. The relative rotations and strains were largest near the ground level, corresponding to the location where large amounts of wall damage would be expected to occur. However, story drift is a better indicator of performance for components of the gravity system (e.g., slab-column connections) and non-structural elements. Figure 6 shows the calculated maximum story drift along with the height of the structure for a 12-story reference archetype (S12-REF) and a 24-story reference archetype (S24-REF). As expected, the story drifts in the basement are near zero because the basement walls are very stiff. In contrast, the maximum story drifts occur near the top stories, because cantilevered walls accumulate rotations over their height.

For the reference archetypes, Figure 7a shows the median (of 100 motions) of the maximum story drift (computed over the height of each archetype) for all earthquake return period motion sets, where the conditional spectra were derived from the 2014 NSHM. As expected, the median MSD values increased with earthquake return period for all archetypes. For example, the median MSD, averaged for all archetypes, increased from 0.3% for a 475-year return period to 2.9% for a return period of 4,975 years. For a 2,475-year earthquake, the average of the median MSD values for all archetypes was around 2.1%. For comparison, the Tall Building

Initiative (TBI) guidelines (PEER, 2017) specify a mean maximum story drift limit of 3.0% at the MCE$_R$-level shaking, which has a return period close to 2,475-years. Thus, the archetype MSDs are consistent with expectations for the 2014 NSHM hazard for which they were designed.

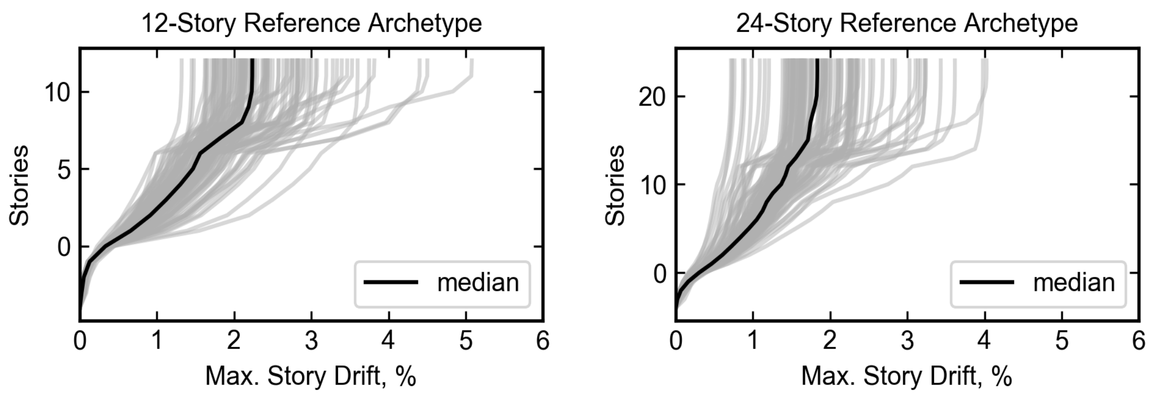

Figure 6. Distribution of story drifts with height for (a) the 12-story reference archetype and (b) the 24-story reference archetype, subjected to motions that represent the 2,475-year earthquake (using the 2018 National Seismic Hazard Model).

The inclusion of basin effects in the 2018 NSHM, and the corresponding increase in ground-motion intensity at all earthquake return periods resulted in increases in median MSD (Figure 7b). For example, the median MSD values averaged for all reference archetypes for the 2,475-year hazard increased from 2.1% using 2014 NSHM motions to 3.7% for 2018 NSHM motions.

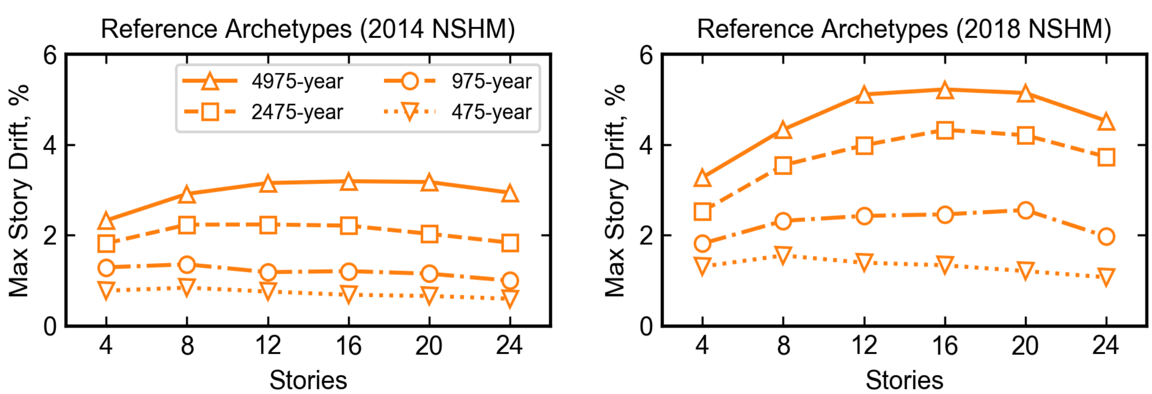

Figure 7. Median of the maximum story drift with respect to archetype number of stories for ground motions selected and scaled to match the conditional spectra at 475-year, 975-year, 2495-year, and 4975-year return periods using: (a) the 2014 version of the National Seismic Hazard Model and (b) the 2018 version of the National Seismic Hazard Model.

Collapse Risk for 2014 and 2018 NSHM

Seismic provisions in the United States target a uniform 1% likelihood of collapse during a 50-year period. Collapse is typically quantified by engineers using the story drift of a structure under intense ground shaking. Haselton et al. (2011b) define collapse as an increase in lateral drift without bounds due to global P-Delta instability. A building may also collapse (or partially collapse) due to the failure of components of the gravity system. Both failure mechanisms were considered in this study.

Drift Capacity of Gravity System

Flat post-tensioned slabs are the most common gravity system in modern RC core-wall residential structures. In this paper, the failure of the gravity system was assumed to be triggered by the failure of the slab-column or slab-wall connection. At these connections, integrity slab reinforcement might delay collapse after punching shear failure due to catenary action; however, it was not possible to model this phenomenon, so punching shear failures were treated as potential "collapses".

Experimental data collected by Hueste et al. (2007 and 2009) were used to evaluate the likelihood of collapse of the gravity system as a function of the slab-column rotation. Hueste et al. found that the drift capacity of slab-column connections depended on the gravity shear ratio (i.e., the ratio of shear load due to gravity loads to concrete shear capacity) and the presence of shear reinforcement. For the reference archetypes, the slab-column connections were assumed to be reinforced with shear studs and had a gravity shear ratio between 0.4 to 0.6. From the data collected by Hueste et al. (2009), the 11 experiments on connections that satisfied these two criteria were conducted by Dilger and Cao, 1991, Dilger and Brown, 1995, and Megally and Ghali, 2000. Figure 8 shows the cumulative distribution (black dots) of the slab-column rotation capacity from those experiments, as well as the corresponding fitted lognormal cumulative distribution (solid curve). The geometric mean of the slab-column rotation capacity was 5.9%, and the lognormal standard deviation (σ_{ln}) was 0.12.

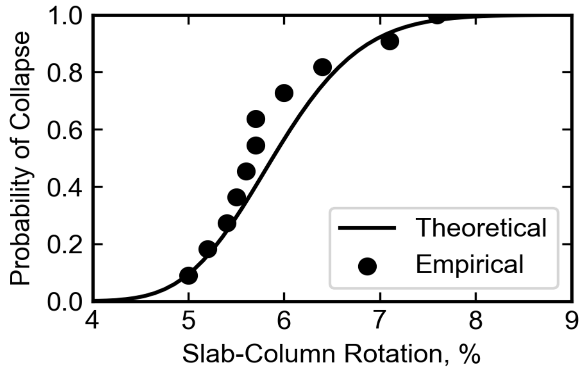

Figure 8. Probability of collapse due to slab-column punching shear failure with respect to the slab-column rotation (for experiments with shear-reinforcements and a gravity shear ratio between 0.4 to 0.6).

Racking Deformations

The engineering demands on the slab-column connections result from the in-plane rotational deformations of the gravity system bays. These rotations are affected by: (1) the cumulative rotation of the core wall at the wall-slab joint at any story, and (2) the added deformations due to racking effects that result from the difference in vertical deformations between the edge of the wall and the adjacent gravity-system column. These columns were assumed to be located on the perimeter of the building for the archetype considered here, as shown in Figure 3.

The total relative rotation between the slab-column and edge-of-wall (due to the combination of these effects) can be computed as the maximum story drift (MSD), amplified by a racking factor, γ_{rack}. Assuming rigid-body rotation of the wall, and assuming no axial shortening in the gravity system columns, the slab-column rotation, SCR, can be approximated as (Charney 1990):

$$SCR = \gamma_{rack}\, MSD = \left(1 + \frac{l_w}{2l_{bay}}\right) MSD \qquad (1)$$

where l_w is the length of the central core, and l_{bay} is the distance between the face of the core wall and the centerline of the gravity columns. The length of the core relative to the length of the gravity system bay (for a constant 30.5 m, 100 ft, floor width) varied among the archetypes. Consequently, γ_{rack} varied among the archetypes from 1.14 (Archetype S4-REF) to 1.45 (Archetype S24-S150).

Collapse Probability

For each archetype and ground-motion set, the collapse probabilities at each level of intensity were computed considering the variability in the slab-column rotations demands (Eq. 1) calculated from the maximum story drift demands and the variation in slab-column rotation capacity:

$$P[C|motion\ set] = \frac{1}{N}\sum_{i=1}^{N} P[C\ |SCR_i] \tag{2}$$

where N corresponds to the number of motions in each earthquake intensity ground-motion set (i.e., 100 motions in each return period stripe), and $P[C|SCR_i]$ is the probability of collapse given the slab-column rotation (SCR, Figure 8) observed from the *i*th motion within that set. It should be noted that the probability of collapse was taken as 1.0 in cases where a global P-Delta instability occurred.

The collapse probabilities (Eq. 2) for each archetype and intensity stripe ground-motion set are shown in Figure 9. As expected, the trends were similar to Figure 7 (which shows median MSD values); the collapse probability increased with earthquake return periods for all archetypes. The inclusion of basin effects in the 2018 NSHM (Figure 9b) greatly increased the collapse probability over those calculated for the 2014 NSHM (Figure 9a). For example, the collapse probability for the 20-story archetype increased from 0.42% (2014) to 38% (2018) for a 2,475-year return period event.

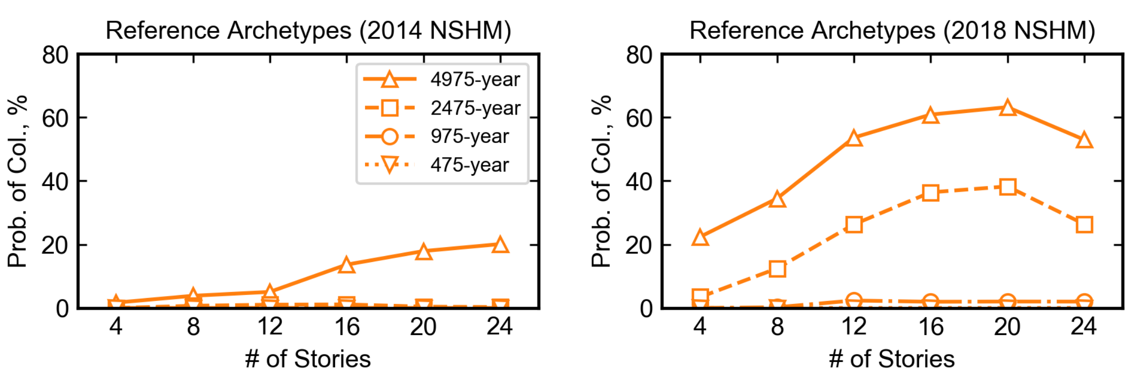

Figure 9. Probability of collapse with respect to archetype number of stories for ground motions selected and scaled to match the conditional spectra at 475-year, 975-year, 2495-year, and 4975-year return periods using: (a) the 2014 version of the National Seismic Hazard Model and the (b) 2018 version of the National Seismic Hazard Model.

50-Year Collapse Risk

ASCE 7-16 (ASCE, 2016) targets a maximum collapse probability of 1% in the 50-year design life of regular buildings. To compare the results obtained above with this target, the annual rate of collapse ($\lambda_{collapse}$), considering the full range of expected shaking intensities from all earthquake sources that contribute to the seismic hazard was computed. Figure 10 shows the probability of collapse for the 8-story, 16-story, and 24-story archetypes with respect to earthquake return period for each ground-motion set (shown using the symbols), for the 2014 NSHM (Figure 10a) and 2018 NSHM (Figure 10b). The figure also shows smooth curves that represent a fitted lognormal distribution of the data points.

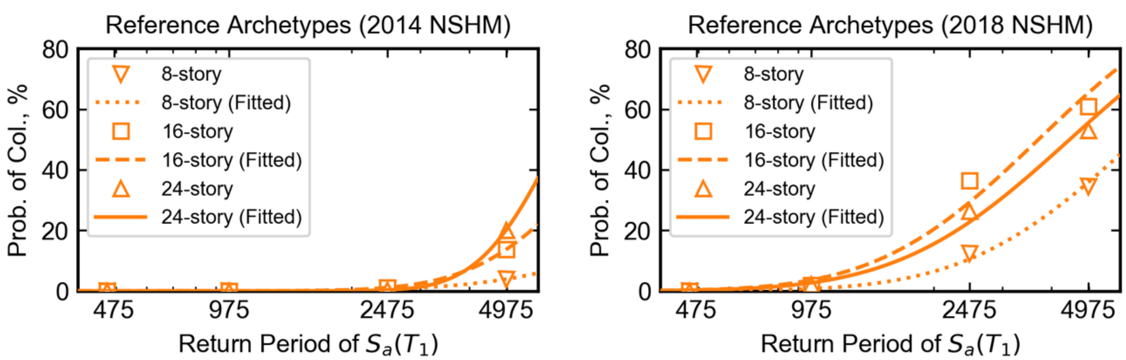

Figure 10. Probability of collapse with respect to earthquake return period for the 8-story, 16-story, and 24-story ASCE 7-16 archetypes evaluated using the (a) 2014 National Seismic Hazard Model and (b) 2018 National Seismic Hazard Model.

A cumulative lognormal distribution was fit using maximum likelihood estimation procedure (Baker 2015) to the conditional probabilities of collapse (expressed in terms of $S_a[T_1]$) and combined with the hazard curve to compute the annual rate of collapse using the following equation:

$$\lambda_{collapse} = \int_{x} P[C|\, IM = x]\, |d\lambda_{IM}(x)| \quad (3)$$

where P[C|IM=x] is the collapse fragility of the archetype with respect to the intensity measure (IM) of interest (in this case $S_a[T_1]$), which is computed using Equation 2 from the set of 100 motions corresponding to IM=x. $\lambda_{IM}(x)$ is the annual rate of exceedance (λ) for $IM = x$, which can be obtained from a ground-motion hazard curve. It should be noted that cases where a maximum likelihood estimation procedure failed to converge (due to near-zero collapse probabilities), a collapse fragility function was predicted by minimizing the sum of square errors between the observed and predicted collapse probability for every intensity stripe (Baker 2015).

The collapse risk in 50 years for each archetype was computed using $\lambda_{collapse}$ assuming a Poisson distribution (i.e., $1\text{-}e^{-\lambda collapse\ t}$, where t was taken as 50 years). Figure 11 shows the 50-year collapse risk for all the reference archetypes using both the 2014 NSHM (hollow square) and 2018 NSHM (hollow triangle). For all archetypes, the average 50-year collapse risk computed using the 2014 and 2018 NSHM were on average equal to 0.5% and 1.3%, respectively. This difference in collapse risk between the NSHM versions indicates that the inclusion of basin effects is critically significant, and results in large increases in collapse risk.

Accounting for Uncertainty due to Material, Design, & Modelling

The probabilities of collapse shown in Figures 9 and 10 were calculated assuming that the record-to-record variability was accounted for with the use of 100 motions, and the variability in the drift capacity was accounted for by the variability in the slab-column rotational capacities measured in experiments (Figure 8, $\sigma_{\ln}$ = 0.12). The resulting record-to-record variability is estimated as the standard deviation in the fitted collapse fragility shown in Figure 10, and denoted as $\sigma_{ln,RTR}$. However, the estimated $\sigma_{ln,RTR}$ does not account for additional uncertainties related to the materials, design methods, and modelling (FEMA P695). In ASCE 7-16's uniform risk target calculations, it is assumed that the total uncertainty in spectral acceleration at collapse (lognormal standard deviation of a collapse fragility) is equal to 0.60, which includes a contribution from the record-to-record uncertainty assumed to be equal to 0.40 (FEMA P695). If the two sources of uncertainty are uncorrelated, the uncertainty due to materials, design methods, and modelling (FEMA P695) can then be approximated as 0.45 = $\sqrt{0.6^2 - 0.4^2}$ (Marafi et al., 2019c). Therefore, to be consistent with the ASCE 7-16 assumptions, the standard deviation in the fitted collapse fragility (Figure 10) was increased by 0.45 (i.e., $\sigma_{\mathrm{ln,T}} = \sqrt{\sigma_{ln,RTR}^2 + 0.45^2}$).

Figure 11 shows that the 50-year collapse risk increased when the additional uncertainty ($\sigma_{ln,T} = \sqrt{\sigma_{ln,RTR}^2 + 0.45^2}$) was taken into account. For example, the average 50-year collapse risk for all reference archetypes computed using the 2018 NSHM increased from 1.3% (hollow triangle) to 2.1% (solid triangle) when the additional uncertainty was considered.

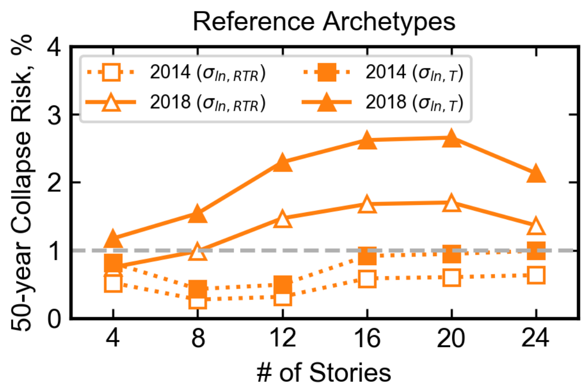

Figure 11. 50-year collapse risk with respect to archetype number of stories for the seismic hazard derived from the 2014 National Seismic Hazard Model and 2018 National Seismic Hazard Model accounting for only record-to-record uncertainty ($\sigma_{ln,RTR}$) and accounting for additional material, design, and modeling uncertainty ($\sigma_{ln,T}$).

Contributions to Collapse Risk

The collapse mechanisms associated with global instability and punching-shear failure both contributed to the 50-year collapse risk. Figure 12a shows that at least 73% of the total 50-year collapse risk was attributable to a slab-column punching shear failure, and the remainder of the collapse risk was attributed to global instability. The contribution of the collapse risk associated with global instability increased with archetype height because large overturning moments develop from the P-Delta column when the top stories drift laterally (Figure 6). For example, the contribution to the 50-year collapse risk from global instability increased from 0% to 24% from the 4-story to 24-story reference archetypes.

Multiple earthquake source mechanisms contribute to the seismic hazard in the Pacific Northwest. Overall, the interface earthquakes contribute about half of the total risk (Figure 12b). The contribution to the collapse risk associated with interface earthquakes increases with structural period; it is largest for the 24-story reference archetypes, corresponding to 64% of the total 50-year collapse risk (Figure 12b). This increase in collapse risk due to interface earthquakes with structural period is due to the increase in percentage contribution of interface earthquakes in the seismic hazard intensity at longer periods.

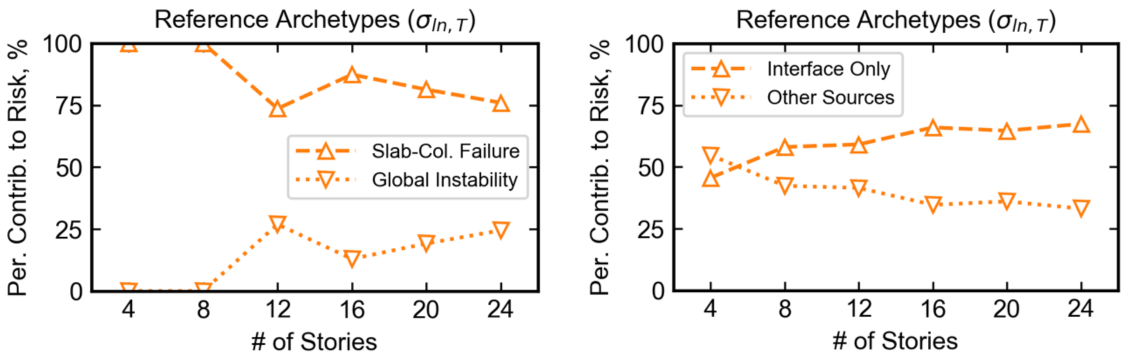

Figure 12. 50-year collapse risk deaggregation showing the (a) contribution of slab-column punching shear failure and global instability and (b) contribution of earthquake source mechanism with respect to archetype number of stories using the 2018 National Seismic Hazard Model.

Design Strategies to Reduce Collapse Risk

Engineers could adopt a variety of design strategies to account for the increase in hazard represented from the 2014 to 2018 NSHM, and reduce the 50-year collapse risk to less than 1%.

Design Strategy #1. Increasing Design Lateral Forces

One strategy for reducing collapse risk is to increase the seismic design lateral force of the structure (i.e., structure's strength). Figure 13a shows the 50-year collapse risk for the reference archetypes redesigned using a 25% increase in ASCE 7-16 design loads (archetype ID designated with a -S125 in Table 1) and a 50% increase in design loads (designated with a -S150). Increasing the design loads by 25% resulted in a reduction in the average 50-year collapse risk from 2.1% (reference archetypes) to 0.90%. A 50% increase in design loads reduced the mean collapse risk further to 0.77%. This result is consistent with the increase in spectral acceleration values observed in the uniform hazard spectrum (UHS) derived from the 2018 NSHM (Figure 2), which was on average equal to 50% for the period ranges of the buildings.

There are material cost and architectural consequences for increasing the seismic design lateral forces. Archetypes designed to a higher seismic force had core wall sizes and reinforcement ratios that were larger than their reference archetype counterparts. Figure 14 shows that the shear wall cross-sectional area at ground level (Figure 14a) and reinforcing steel area at ground level (Figure 14b), as a percentage of the total floor area, increased for all archetypes redesigned with a 50% increase in design lateral forces (-S150 archetypes). For example, the shear wall area increased from 2.0% to 4.5% of the floor area for the 24-story archetype. Similarly, the reinforcing steel area in the wall as a percentage of the total floor area also increased, from 0.0254% to 0.0313%.

In core-wall buildings, the floor area located outside the core has a higher value than floor area enclosed by the core. This consideration is important because one of the consequences of increasing design lateral forces is an increase in floor area devoted to the concrete core. Figure 14c shows the percentage of floor space devoted to the concrete core, assuming a 1.83 m (6 ft) gap between the flanges of the two C-shaped walls (see Figure 3). As expected, the size of the concrete core increased with increased design spectral acceleration (Figure 14c). For example, increasing the design force by 50% for the 24-story archetype doubled the overall core wall area (from 6% to 12% of the total floor area). For archetypes taller than 8 stories, the enclosed core area increased from an average of 3.9% to an average of 6.9% for the -S150 archetypes relative to the reference archetypes.

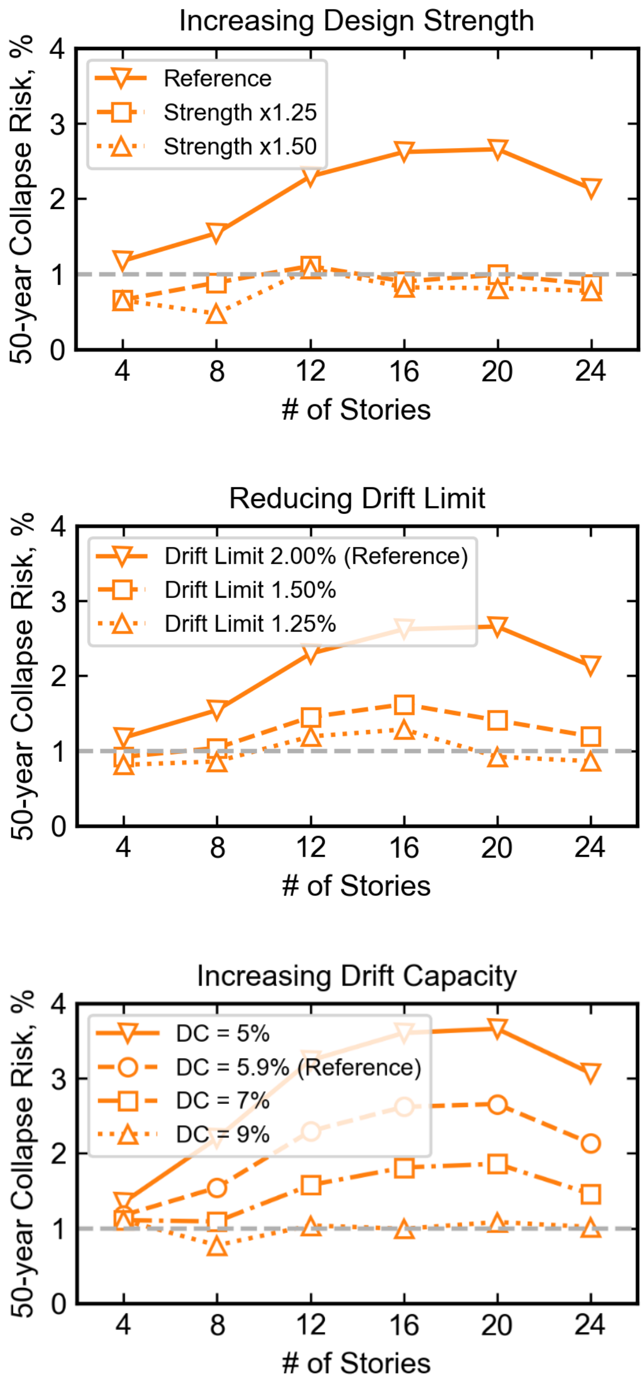

Figure 13. 50-year collapse risk with respect to archetype number of stories using the 2018 National Seismic Hazard Model for (a) various levels of archetype design lateral forces, (b) various levels of archetype design drift limits, and (c) various levels of gravity system drift capacity.

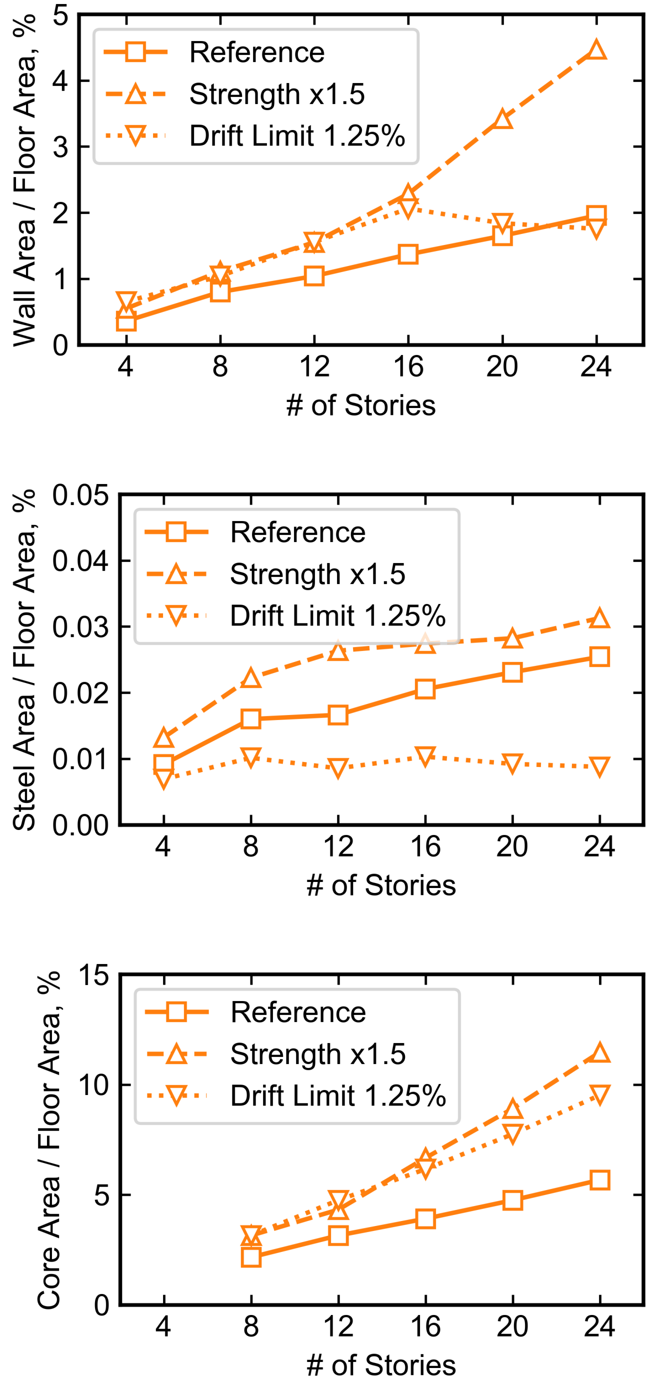

Figure 14. Impacts of increasing design lateral forces or reducing design drift limit on the (a) longitudinal reinforcing steel area, (b) concrete wall cross-sectional area, and (c) a concrete core wall enclosed area as a percentage of the floor area with respect to archetype number of stories.

Design Strategy #2. Decreasing Allowable Drift

Increasing the stiffness of the walls is another strategy to reduce the likelihood of collapse. This increase is achievable by designing archetypes to meet a lower drift limit while maintaining similar design lateral forces to the reference archetypes. Figure 13b shows the collapse risks for reference archetypes (originally designed to meet a 2% limit) that were redesigned to meet a lower drift limit of 1.5% (designated with a -D150) or 1.25% (-D125). As expected, reducing the drift limit reduced the average 50-year collapse risk from 2.1% (reference) to 1.3% and 1.0% for the 1.5% and 1.25% drift limit designs, respectively.

Reducing the design drift limit to 1.25% led to a 36% increase in the wall cross-sectional area on average for all archetypes designed (Figure 14b). As expected, the enclosed core area for archetypes larger than 8-stories also increased, by 57% on average (Figure 14c). In contrast, the reinforcement area in the core wall was reduced (by 48% on average), because the increase in core wall size resulted in a larger moment arm, requiring less reinforcing steel area to achieve a similar strength. In addition, increasing the core size relative to the reference archetypes resulted in a smaller floor area outside the core.

Designing for a lower drift limit is a common seismic design practice. For example, tall buildings in Seattle are often initially proportioned to meet lower drift targets, so that they will satisfy the performance criteria (e.g., Tall Building Initiative). Additionally, engineers often design for lower drift limits to meet the requirements of non-structural components, such as the building facade system (Structural Engineers Association of Washington, personal correspondence, January 9th, 2018).

Design Strategy #3. Increasing Drift Capacity of Gravity System

To reduce the collapse risk associated with slab-column failures, engineers could increase the rotational drift capacity of the slab-column connection. Zhou and Hueste (2017) summarized various slab-column experiments and found that the drift capacity can be increased by: (1) increasing the shear-stress capacity (Dechka, 2001), (2) increasing the length of the shear-stud rails (Brown, 2003), (3) increasing the concentration of top flexural reinforcement (Brown, 2003), and/or (4) increasing the nominal concrete compressive strength (Park et al., 2012).

Figure 13c recomputes the 50-year collapse risk for a series of assumptions for the slab-column connection drift capacity. As expected, increasing the drift capacity reduced the collapse risk for all archetypes. For example, increasing the drift capacity from 5.9% (reference archetype) to 9% (solid line in Figure 13b) decreased the 50-year collapse risk from an average (for all archetypes) of 2.1% to 1.1%.

Increasing the drift capacity does not increase the wall area, longitudinal steel in the walls, nor the enclosed floor area of the core. However, there would likely be additional costs due to additional reinforcement and the decrease in constructability of the slab-column and slab-wall connections to accommodate larger drift capacities.

Design Strategy #4. Combining Strength or Drift Limits with Drift Capacity

Engineers could also mitigate collapse risk by combining design strategies. Figure 15 shows the average (for all archetypes) 50-year collapse risk with respect to the gravity system drift capacity for the reference archetypes and those designed for a higher lateral force (Figure 15a) and reduced drift limit (Figure 15b). To satisfy the target of a maximum 50-year collapse risk of 1%, the drift capacities would need to exceed 9.0% if the reference archetype walls were used (Figure 15a). The drift capacity would only need to be 5.7% and 5.3% for archetypes redesigned with a 25% and 50% increase in design lateral forces, respectively. Alternatively, engineers could also increase the drift capacities to 6.9% and 6.1% if the reference archetypes were redesigned for 1.5% and 1.25% drift limits, respectively (Figure 15b).

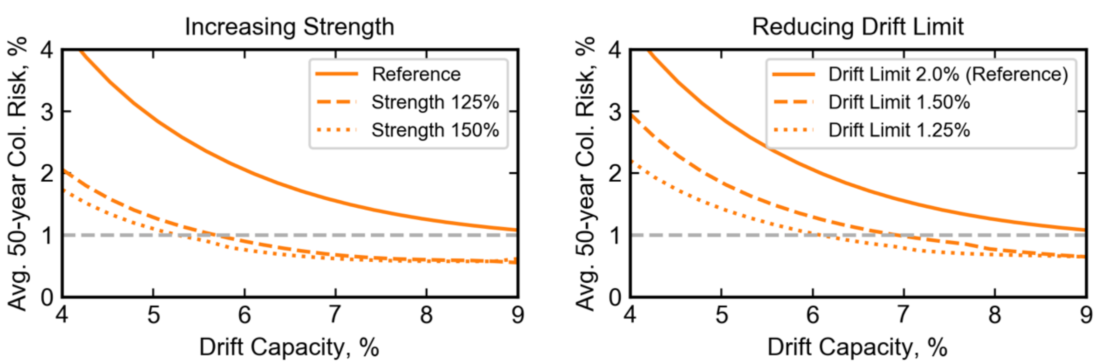

Figure 15. Average 50-year collapse risk with respect gravity system drift capacity using the archetypes with (a) higher design lateral forces and (b) archetypes designed with a reduced drift limit.

Accounting for Simulated M9 CSZ Ground Motions in Collapse Risk

The collapse risk assessments computed previously would change if the simulated **M**9 CSZ ground-motions were used to represent the subduction interface portion of the seismic hazard because: (1) the 2018 NSHMs use basin amplification factors derived from crustal earthquakes (using NGA-West-2 GMMs, Bozorgnia et al., 2014) that are different from amplifications expected during subduction earthquakes (Marafi et al., 2017), and (2) the target conditional spectra (used for each intensity stripe in MSA) used spectral acceleration correlation functions that did not necessarily consider sites located on deep basins.

Figure 16 compares the 50th percentile and 84th percentile for the simulated **M**9 ground-motions in Seattle with the lognormal mean (and mean plus one standard deviation) for the BC-Hydro ground-motion model (Abrahamson et al., 2016), as modified to include basin effects as per the 2018 NSHM (USGS, 2018). The basin amplification terms used in the 2018 NSHM are derived from GMMs for crustal earthquakes, which at periods longer than 1 s tend to be smaller than the M9 simulations (Frankel et al., 2018; Marafi et al., 2019b) (and those observed in subduction earthquakes in Japan [Marafi et al., 2017]).

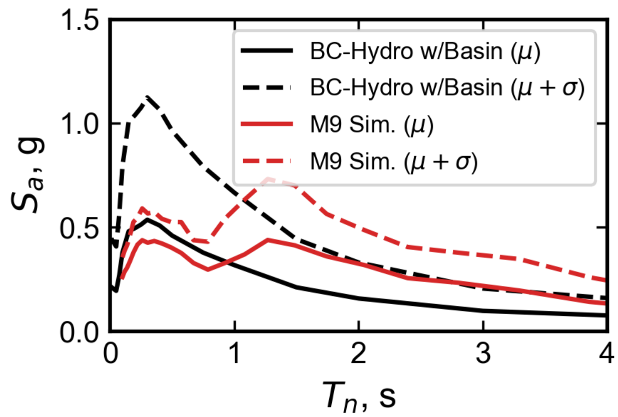

Figure 16. Response spectra for simulated M9 CSZ ground motions for Seattle and the BC-Hydro (Abrahamson et al., 2018) ground-motion model prediction considering basin effects.

In addition, Marafi et al. (2019b, 2019c) found that simulated ground motions for an **M**9 Cascadia Subduction Zone earthquake (Frankel et al., 2018) were particularly damaging for structures, because: (i) the spectral shapes were more damaging than those typically considered in the design of tall buildings using the MCE$_R$ conditional spectra, and (ii) the duration of shaking was much longer than crustal motions typically considered to evaluate structural systems (FEMA P695). For example, the 5-95% significant durations were approximately 115 s for the simulated **M**9 motions (Marafi et al., 2019c) in Seattle, whereas the interface portion of the selected motions for the 2,475-year return period had an average significant duration of about 83 s. These characteristics are not considered in the NSHM and current building code provisions. Other researchers (e.g., Chandramohan, 2016) have proposed adjusting the equivalent lateral force procedures used in ASCE 7 to account for the effects of duration and spectral shape.

Methodology for Incorporating Simulations into Collapse Risk

The portion of the collapse risk attributable interface earthquakes was recomputed using the thirty simulated **M**9 CSZ scenarios by Frankel et al. (2018a). The assumptions embedded in these scenarios were varied to be consistent with the source variability used in the NSHM logic trees for a full rupture of the Cascadia Subduction zone. The annual rate of collapse from the suite of simulated **M**9 earthquakes was computed as:

$$\lambda_{col.,M9} = \lambda_{M9} \sum_{n=1}^{30} \mathrm{P}[Col|N = n]P[N = n] \tag{4}$$

where λ_{M9} corresponds to the annual rate for an **M**9 CSZ earthquake (i.e. reciprocal of the earthquake return period, 1/526 yr^{-1},), and P[$Col|N=n$] is a cumulative lognormal distribution function for the probability of collapse (considering material, design, and modelling uncertainty) given the *n*th simulated earthquake scenario, considering all thirty M9 scenarios, and P[$N=n$]=1/30 is the relative probability of occurrence of the *n*th scenario (each of the 30 simulated scenarios are assumed to be equally probable). The annualized collapse risk from the simulated **M**9 earthquakes was then added to the portion of the annualized collapse risk considering all other earthquake sources and magnitudes:

$$\lambda_{col.,total,wM9} = \lambda_{col.,total} - \lambda_{col,interface} + \lambda_{col.,M9} \tag{5}$$

where $\lambda_{col.,total}$ was computed previously using the NSHM motions and Eq. 3, $\lambda_{col.,M9}$ was computed using Eq 4, and $\lambda_{col.,interface}$ was the deaggregated portion of the total NSHM-based collapse risk ($\lambda_{col.,total}$) associated with interface earthquakes (Figure 12b).

Note that the simulations by Frankel et al. (2018a) only considered variations of an **M**9 event; in reality, the NSHM assumes that the magnitude of a large interface earthquake could vary between **M**8.6 to **M**9.3 (USGS, 2018). This paper used the **M**9 simulations to represent the full range of large-magnitude events.

Collapse Risks for Reference and Redesigned Buildings

Figure 17 shows that the average (for all reference archetypes) 50-year collapse risk increased from 2.1% to 2.8% when the simulated **M**9 motions were considered. For the reference archetypes, the drift capacities would need to exceed 9% (from the current median value of 5.9%) to satisfy the 1% in 50-year collapse risk target, as shown in Figure 18. Alternately, if the archetypes were designed either with a 25% or 50% increase in design lateral forces, the drift capacity would only need to be 5.9% and 5.7%, respectively (Figure 18a).

Redesigning the archetypes with a 1.5% and 1.25% drift limit would require mean drift capacities of 7.2% and 7.0% to meet the 1% collapse target in 50-years (Figure 18b).

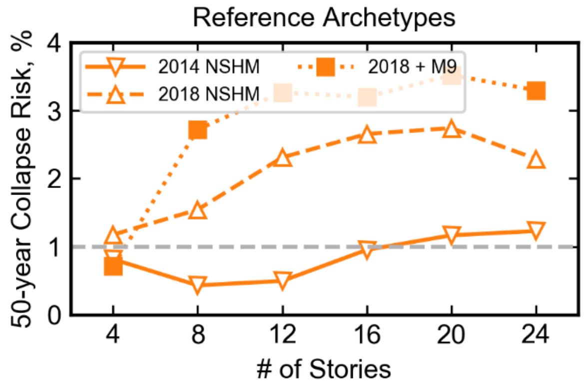

Figure 17. 50-year collapse risk with respect to # of stories considering (1) using the 2014 National Seismic Hazard Model, (2) 2018 National Seismic Hazard Model, and (30 the M9 CSZ scenarios and the 2018 National Seismic Hazard Model for all other earthquake sources.

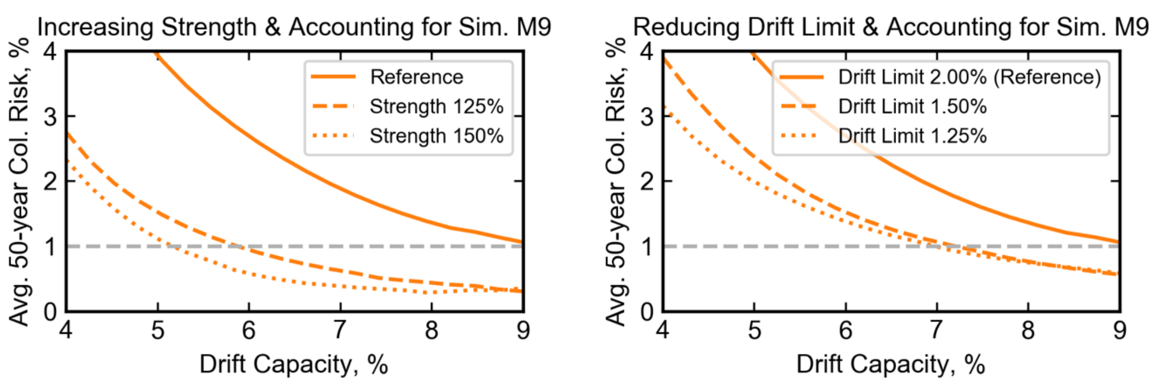

Figure 18. Average 50-year collapse risk considering the simulated M9 earthquake scenarios with respect to drift capacity for archetypes (a) designed with higher design lateral forces and (b) designed with a reduced drift limit.

Conclusions

This study has shown that basin amplification of ground motions can greatly increase the collapse risks of RC wall buildings not designed for such basin effects. The estimated collapse risk further increases when the results of physics-based simulations of large-magnitude interface earthquake were considered. The effectiveness and consequences of adopting several design strategies to reduce the collapse risk were also investigated.

The inclusion of basin effects in the 2018 National Seismic Hazard Model (NSHM) resulted in an increase in long-period spectral accelerations for sites located on deep basins. For Seattle, this increase in spectral acceleration was particularly significant, around 50% greater than the 2014 NSHM version for periods between 0.5 s to 1.5 s (Figure 2).

The impact of basin effects was evaluated for a series of building archetypes, ranging from four to 24 stories, representing modern residential concrete wall buildings in Seattle. Archetypes were developed to reflect a design that satisfies the minimum requirements by ASCE 7-16 code provisions. The archetypes were only evaluated in the uncoupled wall direction where maximum story drifts and collapse probabilities were computed using nonlinear dynamic analysis and a slab-column fragility function that was based on rotation derived from experimental data (Figure 8). The numerical models included additional uncertainty due to modelling, design, and material properties that are consistent with the assumptions in ASCE 7-16 provisions.

The results of a series of multiple stripe analyses showed that the 50-year collapse risk for the reference archetypes increased from 0.7% to 1.8% on average when basin effects were considered in the 2018 NSHM. To reduce the risk of collapse to the 1% target, it was shown that engineers could: (a) increase the ASCE 7-16 design lateral forces by 25% (Figure 13a), (b) reduce the design drift limit from 2.0% to 1.25% (Figure 13b), or (c) increase the gravity system slab-column connection rotational capacity to exceed 9% (Figure 13c). Considering the results from simulations of **M**9 CSZ earthquakes (Frankel et al., 2018a), the average risk of collapse increased to 2.7% for the reference archetypes. To reach the 1% target in this case, it would be necessary to make a combination of changes in the design lateral forces, allowable drift ratios or rotational capacities of the slab-column connections, because the simulated motions had more damaging ground-motion characteristics (Marafi et al., 2019b, c) not currently reflected in building design provisions.

There are economic implications for these design strategies. For example, increasing the design lateral forces increased the amount of concrete and reinforcing steel in the shear walls and increased the floor area enclosed by the core wall (Figure 14), thus reducing the amount of useable floor space outside the core. Reducing the drift limit increased the core wall size and enclosed core area but reduced the total steel area. Increasing the drift capacity of the gravity system would likely result in additional construction costs.

Acknowledgments

The authors would like to acknowledge Art Frankel and Erin Wirth for sharing the results of their simulations of M9 CSZ interface earthquakes. The earthquake engineering committee of the Structural Engineering Association of Washington is also thanked for providing feedback on the development of the building archetypes. This research was funded by the National Science Foundation under Grant No. EAR-1331412. The computations were facilitated through the use of advanced computational, storage, and networking infrastructure provided by Texas Advanced Computing Center at the University of Texas at Austin and NSF Grant No. 1520817 (NHERI Cyberinfrastructure). The authors would also like to thank the two anonymous reviewers for providing thoughtful comments and suggestions that improved the quality of the manuscript. Any opinion, findings, and conclusions or recommendations expressed in this material are those of the authors and do not necessarily reflect the views of the collaborators or sponsoring agencies.

References

Aagaard, B. T., Graves, R. W., Rodgers, A., Brocher, T. M., Simpson, R. W., Dreger, D., Petersson, N. A., Larsen, S. C., Ma, S., and Jachens, R. C. (2010). "Ground-Motion Modeling of Hayward Fault Scenario Earthquakes, Part II: Simulation of Long-Period and Broadband Ground Motion Modeling of Hayward Fault Scenario Earthquakes, Part II." *Bulletin of the Seismological Society of America*, 100(6), 2945–2977.

Abrahamson, N., Gregor, N. and Addo, K. (2016). "BC Hydro ground motion prediction equations for subduction earthquakes." *Earthquake Spectra*, 32(1), pp.23-44.

American Concrete Institute (ACI). (2014). "318-14: Building Code Requirements for Structural Concrete and Commentary."

ASCE. (2017). *Minimum Design Loads and Associated Criteria for Buildings and Other Structures, ASCE/SEI 7-16*. American Society of Civil Engineers, Reston, VA.

Atwater, B. F., Nelson, A. R., Clague, J. J., Carver, G. A., Yamaguchi, D. K., Bobrowsky, P. T., Bourgeois, J., Darienzo, M. E., Grant, W. C., Hemphill-Haley, E., Kelsey, H. M., Jacoby, G. C., Nishenko, S. P., Palmer, S. P., Peterson, C. D., and Reinhart, M. A. (1995). "Summary of Coastal Geologic Evidence for Past Great Earthquakes at the Cascadia Subduction Zone." *Earthquake Spectra*, 11(1), 1–18.

Baker, J. W. (2011). "Conditional Mean Spectrum: Tool for Ground-Motion Selection." *Journal of Structural Engineering*, 137(3), 322–331.

Baker, J. W. (2015). "Efficient Analytical Fragility Function Fitting Using Dynamic Structural Analysis." *Earthquake Spectra*, 31(1), 579–599.

Baker, J. W., and Jayaram, N. (2008). "Correlation of Spectral Acceleration Values from NGA Ground Motion Models." *Earthquake Spectra*, 24(1), 299–317.

Bijelić, N. (2018). "Utilization of physics-based simulated earthquake ground motions for performance assessment of tall buildings." Stanford University.

Bozorgnia, Y., Abrahamson, N. A., Atik, L. Al, Ancheta, T. D., Atkinson, G. M., Baker, J. W., Baltay, A., Boore, D. M., Campbell, K. W., Chiou, B. S.-J., Darragh, R., Day, S., Donahue, J., Graves, R. W., Gregor, N., Hanks, T., Idriss, I. M., Kamai, R., Kishida, T., Kottke, A., Mahin, S. A., Rezaeian, S., Rowshandel, B., Seyhan, E., Shahi, S., Shantz, T., Silva, W., Spudich, P., Stewart, J. P., Watson-Lamprey, J., Wooddell, K., and Youngs, R. (2014). "NGA-West2 Research Project." Earthquake Spectra, 30(3), 973–987.

Brown, S. J. (2003). “Seismic Response of Slab Column Connections.” Univ. of Calgary, Alberta.

Chandramohan, R. (2016). “Duration of earthquake ground motion: Influence on structural collapse risk and integration in design and assessment practice.” Stanford University.

Chang, S. W., Frankel, A. D., and Weaver, C. S. (2014). *Report on Workshop to Incorporate Basin Response in the Design of Tall Buildings in the Puget Sound region, Washington*.

Choi, Y., Stewart, J. P., and Graves, R. W. (2005). “Empirical Model for Basin Effects Accounts for Basin Depth and Source Location.” *Bulletin of the Seismological Society of America*, 95(4), 1412–1427.

City of Seattle Department of Planning and Developments. (2015). “Alternate Design Requirements for Use of Special Reinforced Concrete Shear Walls in Over Height Buildings.” <http://www.seattle.gov/dpd/codes/dr/DR2015-5.pdf> (Apr. 21, 2018).

City of Seattle Department of Planning and Developments. (n.d.). “DR 20-2018, Implementation of March 22, 2018 Basin Amplification Workshop Results.” *2018*.

Crouse, C., Jordan, T. H., Milner, K. R., Goulet, C. A., Callaghan, S., & Graves, R. W. (2018). “Site-Specific MCER Response Spectra for Los Angeles Region based on 3-D Numerical Simulations and the NGA West2 Equations.” *Proceedings of the 11th National Conference in Earthquake Engineering*.

Dechka, D. C. (2001). “Response of Shear-Stud-Reinforced Continuous Slab-Column Frames to Seismic Loads.” Univ. of Calgary, Canada.

Dilger, W. G., and Brown, S. J. (1995). *Earthquake Resistance of Slab-Column Connection*. Zurich, Switzerland.

Dilger, W., and Cao, H. (1991). “Behaviour of Slab-Column Connections under Reversed Cyclic Loading.” *Proceedings of the Second International Conference of High-Rise Buildings*, China, 10.

FEMA (Federal Emergency Management Agency). (2009). *Quantification of Building Seismic Performance Factors*. Redwood, CA.

Frankel, A., Wirth, E., Marafi, N., Vidale, J., and Stephenson, W. (2018). “Broadband Synthetic Seismograms for Magnitude 9 Earthquakes on the Cascadia Megathrust Based on 3D Simulations and Stochastic Synthetics, Part 1: Methodology and Overall Results.” *Bulletin of the Seismological Society of America*, 108(5A), 2347–2369.

Goldfinger, C., Nelson, C. H., Morey, A. E., Johnson, J. E., Patton, J. R., Karabanov, E., Gutiérrez-Pastor, J., Eriksson, A. T., Gràcia, E., Dunhill, G., Enkin, R. J., Dallimore, A., and Vallier, T. (2012). *Turbidite Event History—Methods and Implications for Holocene Paleoseismicity of the Cascadia Subduction Zone*.

Graves, R., Jordan, T. H., Callaghan, S., Deelman, E., Field, E., Juve, G., Kesselman, C., Maechling, P., Mehta, G., Milner, K., Okaya, D., Small, P., and Vahi, K. (2011). “CyberShake: A Physics-Based Seismic Hazard Model for Southern California.” *Pure and Applied Geophysics*, 168(3–4), 367–381.

Gregor, N., Abrahamson, N. A., Atkinson, G. M., Boore, D. M., Bozorgnia, Y., Campbell, K. W., Chiou, B. S.-J., Idriss, I. M., Kamai, R., Seyhan, E., Silva, W., Stewart, J. P., and Youngs, R. (2014). “Comparison of NGA-West2 GMPEs.” *Earthquake Spectra*, 30(3), 1179–1197.

Haselton, C. B., Liel, A. B., Deierlein, G. G., Dean, B. S., and Chou, J. H. (2011). “Seismic Collapse Safety of Reinforced Concrete Buildings. I: Assessment of Ductile Moment Frames.” *Journal of Structural Engineering*, 137(4), 481–491.

Heaton, T. J., Yang, J., and Hall, J. (2006). “Simulated performance of steel moment-resisting frame buildings in the 2003 Tokachi-Oki earthquake.” Bull. Earthq. Res. Inst., Univ. Tokyo, 81, 325–329.

Hueste, M. B. D., Browning, J., Lepage, A., and Wallace, J. W. (2007). “Seismic Design Criteria for Slab-Column Connections.” *ACI Structural Journal*, 104(4), 448–458.

Hueste, M. B. D., Kang, T. H.-K., and Robertson, I. N. (2009). “Lateral Drift Limits for Structural Concrete Slab-Column Connections Including Shear Reinforcement Effects.” *Structures Congress 2009*, American Society of Civil Engineers, Reston, VA, 1–10.

Jalayer, F., and Cornell, C. A. (2009). “Alternative non-linear demand estimation methods for probability-based seismic assessments.” *Earthquake Engineering & Structural Dynamics*, 38(8), 951–972.

Jayaram, N., Baker, J. W., Okano, H., Ishida, H., McCann, M. W. J., and Mihara, Y. (2011). “Correlation of response spectral values in Japanese ground motions.” *Earthquakes and Structures*, 2(4), 357–376.

Jayaram, N., Lin, T., and Baker, J. W. (2011). "A Computationally Efficient Ground-Motion Selection Algorithm for Matching a Target Response Spectrum Mean and Variance." *Earthquake Spectra*, 27(3), 797–815.

Kunnath, S. K., Heo, Y., and Mohle, J. F. (2009). "Nonlinear Uniaxial Material Model for Reinforcing Steel Bars." *Journal of Structural Engineering*, 135(4), 335–343.

Marafi, N. A. (2018). "Impacts of an M9 Cascadia Subduction Zone Earthquake on Structures Located In Deep Sedimentary Basins." University of Washington.

Marafi, N. A., Berman, J. W., and Eberhard, M. O. (2016). "Ductility-dependent intensity measure that accounts for ground-motion spectral shape and duration." *Earthquake Engineering & Structural Dynamics*, GB, 45(4), 653–672.

Marafi, N. A., Eberhard, M. O., Berman, J. W., Wirth, E. A., and Frankel, A. D. (2017). "Effects of Deep Basins on Structural Collapse during Large Subduction Earthquakes." *Earthquake Spectra*, 33(3), 963–997.

Marafi, N. A., Ahmed, K. A., Lehman, D. E., and Lowes, L. N. (2019a). "Variability in Seismic Collapse Probabilities of Solid and Coupled-Wall Buildings." *Journal of Structural Engineering, In-press*.

Marafi, N. A., Eberhard, M. O., Berman, J. W., Wirth, E. A., and D., F. A. (2019b). "Impacts of Simulated M9 Cascadia Subduction Zone Motions on Idealized Systems." *Earthquake Spectra, In-press*.

Marafi, N. A., Makdisi, A. J., Eberhard, M. O., and Berman, J. W. (2019c). "Performance of RC Core-Walls during Simulated M9 Cascadia Subduction Zone Earthquake Scenarios." *Journal of Structural Engineering, In-review*.

McKenna, F. (2016). "OpenSees." Pacific Earthquake Engineering Research Center, <http://opensees.berkeley.edu/> (Apr. 24, 2018).

Megally, S., and Ghali, A. (2000). "Punching Shear Design of Earthquake-Resistant Slab-Column Connections." *ACI Structural Journal*, 97(5), 720–730.

Morikawa, N., and Fujiwara, H. (2013). "A New Ground Motion Prediction Equation for Japan Applicable up to M9 Mega-Earthquake." *Journal of Disaster Research*, 8(5), 878–888.

Moschetti, M. P., Hartzell, S., Stephenson, W. J., Angster, S. J., Ramírez-Guzmán, L., and Frankel, A. D. (2017). "3D Ground-Motion Simulations of Mw 7 Earthquakes on the Salt Lake City Segment of the Wasatch Fault Zone: Variability of Long-Period (T≥1 s) Ground Motions and Sensitivity to Kinematic Rupture Parameters 3D Ground-Motion Simulations of Mw 7 Earthquakes on." *Bulletin of the Seismological Society of America*, 107(4), 1704–1723.

Park, H.-G., Kim, Y.-N., Song, J.-G., and Kang, S.-M. (2012). "Lattice Shear Reinforcement for Enhancement of Slab-Column Connections." *Journal of Structural Engineering*, 138(3), 425–437.

Pugh, J. S., Lowes, L. N., and Lehman, D. E. (2015). "Nonlinear line-element modeling of flexural reinforced concrete walls." *Engineering Structures*, 104, 174–192.

Rathje, E. M., Dawson, C., Padgett, J. E., Pinelli, J.-P., Stanzione, D., Adair, A., Arduino, P., Brandenberg, S. J., Cockerill, T., Dey, C., Esteva, M., Haan, F. L., Hanlon, M., Kareem, A., Lowes, L., Mock, S., and Mosqueda, G. (2017). "DesignSafe: New Cyberinfrastructure for Natural Hazards Engineering." *Natural Hazards Review*, 18(3), 06017001.

Petersen, M. D., Moschetti, M. P., Powers, P. M., Mueller, C. S., Haller, K. M., Frankel, A. D., Zeng, Y., Rezaeian, S., Harmsen, S. C., Boyd, O. S., Field, N., Chen, R., Rukstales, K. S., Luco, N., Wheeler, R. L., Williams, R. A., and Olsen, A. H. (2014). Documentation for the 2014 Update of the United States National Seismic Hazard Maps.

USGS (United States Geological Survey). (2018). "Preliminary 2018 Update of the U.S. National Seismic Hazard Model: Overview of Model, Changes, and Implications."

USGS (United States Geological Survey). (2019). "National Seismic Hazard Mapping Project (NSHMP) Code." <https://github.com/usgs/nshmp-haz>.

Wirth, E. A., Chang, S. W., and Frankel, A. D. (2018). "2018 report on incorporating sedimentary basin response into the design of tall buildings in Seattle, Washington:" *U.S. Geological Survey Open-File Report*, (1149), 19.

Wirth, E. A., Frankel, A. D., Marafi, N., Vidale, J. E., and Stephenson, W. J. (2018). "Broadband Synthetic Seismograms for Magnitude 9 Earthquakes on the Cascadia Megathrust Based on 3D Simulations and Stochastic Synthetics, Part 2: Rupture Parameters and Variability." *Bulletin of the Seismological Society of America*, 108(5A), 2370–2388.

Zhou, Y., and Hueste, M. B. D. (2017). "Review of test data for interior slab-column connections with moment transfer." *American Concrete Institute Special Publication*, 315, 141–166.

Appendix

Appendix Table 1. Properties of reference archetype geometry and reinforcement

Archetype	Stories	l_w (in)	b_w (in)	t_w (in)	ρ_l	ρ_v
S4-REF	-1 to 4	144	-	18	-	-
S8-REF	-2 to 3	144	72	24	2.00	4.00
S8-REF	4 to 6	144	72	24	1.00	1.00
S8-REF	7 to 8	144	72	24	0.25	0.25
S12-REF	-3 to 3	180	90	24	1.60	3.20
S12-REF	4 to 6	180	90	24	1.20	1.20
S12-REF	7 to 9	168	90	18	0.70	2.10
S12-REF	10 to 12	168	90	18	0.25	0.25
S16-REF	-3 to 4	204	102	28	1.50	3.50
S16-REF	5 to 8	204	102	28	1.00	1.17
S16-REF	9 to 12	188	102	20	0.60	1.28
S16-REF	13 to 16	188	102	20	0.25	0.25
S20-REF	-3 to 4	228	114	30	1.40	2.77
S20-REF	5 to 8	228	114	30	0.95	1.19
S20-REF	9 to 12	212	114	22	0.70	1.14
S20-REF	13 to 20	212	114	22	0.25	0.25
S24-REF	-3 to 4	252	126	32	1.30	2.74
S24-REF	5 to 8	252	126	32	1.10	1.47
S24-REF	9 to 12	240	126	26	0.80	1.13
S24-REF	13 to 16	240	126	26	0.35	0.25
S24-REF	17 to 24	240	126	26	0.25	0.25

Appendix Table 2. Properties of design strategy #1 archetype geometry and reinforcement

Archetype	Stories	l_w (in)	b_w (in)	t_w (in)	ρ_l	ρ_v
S4-S125	-1 to 4	156	-	20	-	-
S8-S125	-2 to 3	168	84	24	2	4
S8-S125	4 to 6	168	84	24	1.1	1.1
S8-S125	7 to 8	168	84	24	0.3	0.25
S12-S125	-3 to 3	216	108	24	1.55	3.1
S12-S125	4 to 6	216	108	24	1.25	1.25
S12-S125	7 to 9	204	108	18	0.75	2.25
S12-S125	10 to 12	204	108	18	0.25	0.25
S16-S125	-3 to 4	264	132	34	0.9	2.55
S16-S125	5 to 8	264	132	34	0.8	1.48
S16-S125	9 to 12	244	132	24	0.6	1.54
S16-S125	13 to 16	244	132	24	0.25	0.25
S20-S125	-3 to 4	312	156	40	0.68	2.25
S20-S125	5 to 8	312	156	40	0.6	1.31
S20-S125	9 to 12	284	156	26	0.6	1.16
S20-S125	13 to 16	284	156	26	0.25	0.25
S20-S125	17 to 20	276	156	22	0.25	0.25
S24-S125	-3 to 4	360	180	44	0.53	2.51
S24-S125	5 to 8	360	180	44	0.53	1.26
S24-S125	9 to 12	332	180	30	0.55	1.22
S24-S125	13 to 16	332	180	30	0.3	0.25
S24-S125	17 to 24	320	180	24	0.25	0.25
S4-S150	-1 to 4	180	-	22	-	-
S8-S150	-2 to 3	180	90	26	2	2.77
S8-S150	4 to 6	180	90	26	1.3	1.11
S8-S150	7 to 8	180	90	26	0.4	0.25
S12-S150	-3 to 3	216	108	30	1.7	3.36
S12-S150	4 to 6	216	108	30	1.35	1.69
S12-S150	7 to 9	200	108	22	0.9	1.47
S12-S150	10 to 12	200	108	22	0.35	0.25
S16-S150	-3 to 4	276	138	34	1.2	2.69

S16-S150	5 to 8	276	138	34	0.9	1.27
S16-S150	9 to 12	260	138	26	0.65	1.8
S16-S150	13 to 16	260	138	26	0.25	0.25
S20-S150	-3 to 4	324	162	44	0.82	3.02
S20-S150	5 to 8	324	162	44	0.7	1.28
S20-S150	9 to 12	296	162	30	0.7	0.87
S20-S150	13 to 16	296	162	30	0.4	0.25
S20-S150	17 to 20	280	162	22	0.25	0.25
S24-S150	-3 to 4	372	186	50	0.7	2.92
S24-S150	5 to 8	372	186	50	0.6	1.25
S24-S150	9 to 12	344	186	36	0.65	1.27
S24-S150	13 to 16	344	186	36	0.4	0.25
S24-S150	17 to 24	324	186	26	0.25	0.25

Appendix Table 3. Properties of design strategy #2 archetype geometry and reinforcement

Archetype	Stories	l_w (in)	b_w (in)	t_w (in)	ρ_l	ρ_v
S4-D150	-1 to 4	156	-	24	-	-
S8-D150	-2 to 3	168	84	24	1.25	2.5
S8-D150	4 to 6	168	84	24	0.8	0.8
S8-D150	7 to 8	168	84	24	0.25	0.25
S12-D150	-3 to 3	204	102	26	1.02	2.22
S12-D150	4 to 6	204	102	26	0.8	1.13
S12-D150	7 to 9	188	102	18	0.6	1.15
S12-D150	10 to 12	188	102	18	0.25	0.25
S16-D150	-3 to 4	240	120	32	0.72	1.93
S16-D150	5 to 8	240	120	32	0.6	0.8
S16-D150	9 to 12	212	120	18	0.5	0.96
S16-D150	13 to 16	212	120	18	0.25	0.25
S20-D150	-3 to 4	276	138	36	0.53	2.06
S20-D150	5 to 8	276	138	36	0.53	1.03
S20-D150	9 to 12	244	138	20	0.5	0.74
S20-D150	13 to 16	244	138	20	0.25	0.25
S20-D150	17 to 20	248	138	22	0.25	0.25
S24-D150	-3 to 4	300	150	40	0.5	2.18
S24-D150	5 to 8	300	150	40	0.5	1.09
S24-D150	9 to 12	272	150	26	0.55	0.78
S24-D150	13 to 16	272	150	26	0.35	0.25
S24-D150	17 to 24	260	150	20	0.25	0.25
S4-D125	-1 to 4	168	-	28	-	-
S8-D125	-2 to 3	180	90	24	0.97	2.55
S8-D125	4 to 6	180	90	24	0.65	0.85
S8-D125	7 to 8	180	90	24	0.25	0.25
S12-D125	-3 to 3	228	114	28	0.55	1.68
S12-D125	4 to 6	228	114	28	0.5	1.04
S12-D125	7 to 9	204	114	16	0.5	0.85
S12-D125	10 to 12	204	114	16	0.25	0.25
S16-D125	-3 to 4	264	132	32	0.5	2.37

S16-D125	5 to 8	264	132	32	0.5	1.19
S16-D125	9 to 12	232	132	16	0.5	0.85
S16-D125	13 to 16	232	132	16	0.25	0.25
S20-D125	-3 to 4	300	150	24	0.5	1.31
S20-D125	5 to 8	300	150	24	0.5	0.65
S20-D125	9 to 12	292	150	20	0.5	0.74
S20-D125	13 to 16	292	150	20	0.3	0.25
S20-D125	17 to 20	284	150	16	0.25	0.25
S24-D125	-3 to 4	336	168	20	0.5	2.13
S24-D125	5 to 12	336	168	20	0.5	1.07
S24-D125	13 to 16	336	168	20	0.25	0.25
S24-D125	17 to 24	328	168	16	0.25	0.25

Appendix Table 4. Properties of 4-story planar wall archetypes

Archetype	*Stories*	l_{be} *(in)*	$\rho_{l,be}$
S4-REF	-1 to 2	*50*	*0.035*
S4-REF	2 to 4	*42*	*0.023*
S4-S125	-1 to 2	*66*	*0.032*
S4-S125	2 to 4	*66*	*0.020*
S4-S150	-1 to 2	*74*	*0.027*
S4-S150	2 to 4	*74*	*0.018*
S4-D150	-1 to 2	*38*	*0.027*
S4-D150	2 to 4	*38*	*0.017*
S4-D125	-1 to 2	*42*	*0.019*
S4-D125	2 to 4	*34*	*0.015*